PROCEEDINGS A

rspa.royalsocietypublishing.org

Research

Article submitted to journal

Subject Areas:
Fluid mechanics, Applied mathematics, Chemical engineering

Keywords:
Foam improved oil recovery, Pressure-driven growth, Semidiscrete central-upwind scheme, Level set methods

Author for correspondence:
Carlos Torres-Ulloa
e-mail: carlos.torres@uct.cl

Foam-liquid front motion in Eulerian coordinates

C. Torres-Ulloa[1,3], S. Berres[2] and P. Grassia[3]

[1]Departamento de Procesos Industriales, Universidad Católica de Temuco, Rudecindo Ortega 02950, Temuco, Chile
[2]Departamento de Ciencias Matemáticas y Físicas, Universidad Católica de Temuco, Rudecindo Ortega 02950, Temuco, Chile
[3]Department of Chemical and Process Engineering, University of Strathclyde, James Weir Building, 75 Montrose St, Glasgow G1 1XJ, UK

A mathematical model formulated as a system of Hamilton-Jacobi equations describes implicitly the propagation of a foam-liquid front in an oil reservoir, as the zero level set of the solution variable. The conceptual model is based on the "pressure-driven growth" model in Lagrangian coordinates. The Eulerian mathematical model is solved numerically, where the marching is done via a finite volume scheme with an upwind flux. Periodic reinitialization ensures a more accurate implicit representation of the front. The numerical level set contour values are initially formed to coincide with an early-time asymptotic analytical solution of the pressure-driven growth model. Via the simulation of the Eulerian numerical model, numerical data are obtained from which graphical representations are generated for the location of the propagating front, the angle that the front normal makes with respect to the horizontal, and the front curvature, all of which are compared with the Lagrangian model predictions. By making this comparison, it is possible to confirm the existence of a concavity in the front shape at small times, which physically corresponds to an abrupt reorientation of the front over a limited length scale.

THE ROYAL SOCIETY PUBLISHING

1. Introduction

Usually, in an oil well, just a fraction of the oil is extracted using the internal pressure of the reservoir as a driving force [1]. This stage is called primary recovery. Thereafter large amounts of oil remain to be recovered. A secondary technique involves the injection of water into the deposit, in order to maintain a high reservoir pressure [2]. For a third extraction stage there are technologies, processes or mechanisms known as Tertiary or Enhanced Oil Recovery (EOR), the application of which can help to recover additional oil [1]. Enhanced Oil Recovery is defined as the set of methods that use external energy sources or materials to recover oil that cannot be produced by conventional means employed during primary and secondary recovery [3].

One of the techniques for tertiary oil extraction is the use of foam [4]. The foam is created typically by alternate injection of surfactant solution and gas, with finely-textured foam being produced at a propagating front that forms the boundary between surfactant solution and gas, with coarsely-textured foam also being left behind further back [5]. This method uses the fact that the foam (particularly finely-textured foam) is relatively immobile within the oil reservoir, associated with the large force required to drive the foam films through channels in a porous medium [4]. Thus the effective viscosity of the finely-textured foam is much larger than that of the surfactant solution (downstream) or the coarsely-textured foam (upstream). Being less mobile, foam controls the flow of any of the other reservoir fluids, and by extension, to control the overall fluid flow through the reservoir, it is sufficient to control the flow of the foam.

An idealized schematic model that explains the movement of the foam front in the petroleum reservoir was introduced in [5] and [6] (see Figure 1). This model is used as a basis for work developed in [4] and herein.

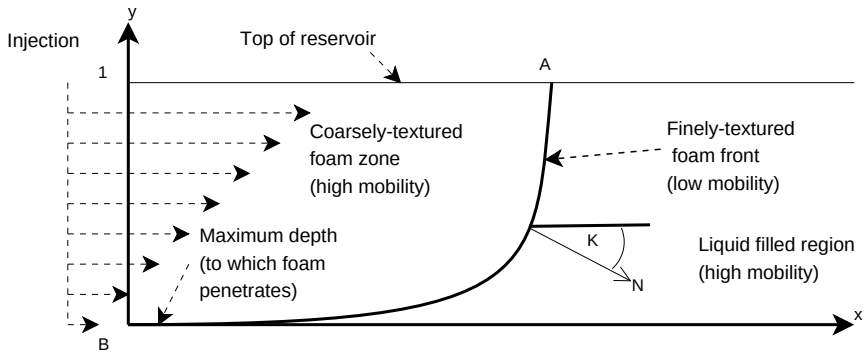

Figure 1. Sketch of the foam-liquid model. The physical domain is expressed in dimensionless form as $x \in [0, \infty)$ and $y \in [0, 1]$. How this model was cast in dimensionless form can be found in [4]. At any location, the front propagates along its local normal direction (where the front normal **n** is at an angle α from the horizontal) at a speed that depends on the depth as well as upon distance the front has propagated. At the top of the domain the foam front forms a right angle ($\alpha = 0$), which physically represents a no penetration condition at the top. As established in [6], at the top (where $y = 1$) the front evolves as $x = \sqrt{2t}$, which is used as boundary condition of the Eulerian model (see also section 3).

As the finely-textured foam front propagates, it pushes liquid (surfactant solution and oil) ahead of it until it ultimately reaches the production well. At the front, the foam is more finely-textured and less mobile. Moreover the front width (i.e. the thickness of the finely-textured zone, and hence the resistance to motion that this zone presents), is proportional to the length of the trajectory through which material points on the front have propagated [4]. In the idealized model presented by [5] and [6], all resistance to the flow is concentrated in the low mobility foam

front, as can be visualized in Figure 1. Moreover, there is a maximum foam penetration depth, which follows from the decaying difference as depth increases between the constant injection pressure and the increasing hydrostatic pressure [4]. At some point, which we denote $y = 0$, this net driving pressure vanishes [4].

Previous model formulations have been Lagrangian (following front material points [4,7–10]). Recently in [7] it was proposed that an Eulerian model might overcome some of the difficulties with the computational simulation of the Lagrangian model, which requires regridding but without any indication of where to place newly added grid points. This issue becomes particularly acute when one recognizes that the pressure-driven growth model can exhibit singularities [4], which physically are regions in which the finely-textured foam front reorients significantly over a small distance. In a Lagrangian scheme one can never be certain whether a singularity computed numerically is really present in the physical model or is merely an artifact of misplacement of newly added Lagrangian grid points. In [7] some preliminary Eulerian data were discussed (and indicated a small concavity in the front shape), but [7] did not describe in detail how those data were obtained. Eulerian simulation thereby detects jumps in the front orientation angle, which are difficult to identify with a Lagrangian model. The purpose of this current paper is to show the reformulation of the Lagrangian model as an Eulerian one (see section 3), to present the numerical implementation of the Eulerian model (which needs to be formulated in terms of two dependent variables rather than just a single one), and to examine Eulerian data in more detail, including a full description of the methodology used to obtain them.

The present work is arranged as follows. In the next section a brief description of the Lagrangian formulation known as the pressure-driven growth model is covered in order to understand the physics of the model. Then in section 3 the general context of the Eulerian solution is introduced, explaining the mathematical formulation for the pressure-driven growth model, using Eulerian coordinates. After that, in section 4 a description is given of the numerical scheme by which the new model was solved. This leads to the results, in section 5, where the comparison between the Lagrangian and Eulerian model is made, using the explicit representation for the front at different times and also measuring the curvature and the orientation angle of the front. The conclusions are given in section 6.

2. Lagrangian model

Although we choose to employ an Eulerian model in this work, originally pressure-driven growth was formulated as a Lagrangian model. We review the Lagrangian model here. As indicated in [4], the idealized Lagrangian model of [5] and [6] is characterized by the following properties:

(i) The petroleum reservoir is geologically homogeneous.
(ii) The model consists of two regions, foam and liquid with a front between them.
(iii) The liquid filled region (bottom right zone in Figure 1) and a region of coarsely-textured foam (top left zone in Figure 1), are assumed to be perfectly mobile in comparison to the finely-textured foam zone close to the front.
(iv) The thickness of the finely-textured zone is much smaller than the trajectory through which the front has moved. Therefore, the zone of finely-textured foam can be considered to be a curve (an idealised representation of an area of comparatively small thickness), which propagates through the petroleum reservoir. Any singularities that the model might predict in the shape of the front correspond physically to the front reorienting itself on a length scale comparable with the thickness of the finely-textured zone.
(v) The finely-textured zone is pushed along by a net driving pressure: At the top boundary of the domain the net driving pressure is maximal and at the lower boundary the net driving pressure is zero.

From the derivation of the model presented in [5] and [6] and realized in [4], the evolution of the front in Lagrangian coordinates is given in dimensionless form by

$$\frac{\mathrm{d}\mathbf{x}}{\mathrm{d}t} = \frac{\Delta P}{s}\mathbf{n}, \quad \Delta P = y, \tag{2.1}$$

where $\mathbf{x} = (x, y)$ corresponds to a point on the front in Cartesian coordinates, s is the length of the trajectory of the points on the front, and ΔP is the driving-pressure difference. Equation (2.1) is just a statement of Darcy's law, recognising that the lowest mobility in the system is at the finely-textured foam front, which is where the bulk of the Darcy pressure drop occurs, making it no longer necessary to solve a conventional two-phase flow Darcy model [5]. In our dimensionless coordinate system, the specification $\Delta P = y$ is given by [4], and reflects the fact that net driving pressure (injection pressure less hydrostatic pressure) grows with the height.

The front orientation angle α is defined to be between the front normal and a horizontal line,

$$\tan(\alpha) = \mathrm{d}x/\mathrm{d}y, \tag{2.2}$$

or equivalently $\alpha = \arctan(\mathrm{d}x/\mathrm{d}y)$. The notational convention here from [7] is that $\mathrm{d}/\mathrm{d}t$ denotes a time derivative following a material point, whereas $\mathrm{d}/\mathrm{d}y$ denotes a spatial derivative along the foam front from material point to material point. If the normal $\mathbf{n}$ is expressed in terms of the angle α as $\mathbf{n} = (\cos(\alpha), -\sin(\alpha))$, then the model becomes

$$\frac{\mathrm{d}x}{\mathrm{d}t} = \frac{y}{s}\cos(\alpha), \tag{2.3}$$

$$\frac{\mathrm{d}y}{\mathrm{d}t} = -\frac{y}{s}\sin(\alpha). \tag{2.4}$$

The length of the trajectory s evolves according to

$$\mathrm{d}s/\mathrm{d}t = \sqrt{\left(\mathrm{d}x/\mathrm{d}t\right)^2 + \left(\mathrm{d}y/\mathrm{d}t\right)^2}. \tag{2.5}$$

Inserting the model equations (2.3) and (2.4) into (2.5) gives

$$\mathrm{d}s/\mathrm{d}t = y/s. \tag{2.6}$$

The Lagrangian model for the foam-liquid front propagation consists of equations (2.1) and (2.6).

A set of asymptotic analytical solutions of the Lagrangian pressure-driven growth model developed in [4], [7] and [9] have shown that over time a gap appears between the top boundary and material points on the front initially near the top boundary, and that is an essential part of the physics (material points slightly below the top boundary move downwards as well as sideways). This situation is described in more detail in Appendix A and B. When developing a Lagrangian numerical scheme, one does not know a priori where (in order to fill the gap) those newly injected points should be placed. If they are placed in the wrong position to start with, then the subsequent evolution of the front may also be wrongly predicted, which is potentially problematic from the point of view of the Lagrangian model. To address this issue, a method is sought to describe the front evolution without the need to handle injected points. It is proposed to reformulate the model in Eulerian coordinates, since this type of formulation does not require a continuous monitoring of the material points. Instead it fixes the physical domain and measures how the front evolves through that domain.

3. Eulerian model

In this section the Eulerian model for foam-liquid front propagation is presented and its connection to a Lagrangian model is shown. The Eulerian model is expressed using the

Hamilton-Jacobi equation [11], which in general terms can be written as

$$\phi_t + H(\nabla\phi) = 0, \tag{3.1}$$

where $\phi = \phi(\mathbf{x}, t)$, $\mathbf{x} \in \mathbb{R}^m$, and the Hamiltonian H depends on the gradient $\nabla\phi$. The front is implicitly represented as a zero level set where $\phi = 0$.

To simulate the propagation of the implicit representation for propagation fronts, we make use of the Level Set Method [12], an established robust technique to simulate the evolution of curves. The method can be used to solve problems that involve the movement of curves and boundaries, for example the propagation of fire fronts [12], surface reconstruction [13], and also to predict the deformation patterns of multi-layered materials [14]. The method evolves a function $\phi = \phi(\mathbf{x}, t)$ with special focus on a manifold of co-dimension one (i.e. a surface in a 3D domain and a curve in a 2D domain), which is implicitly described as a zero level set where $\phi = 0$. These manifolds propagate in a normal direction with a specified velocity [15]. We adopt a sign convention in which the direction of front propagation is taken to be in the $+\nabla\phi$ direction, rather than in the $-\nabla\phi$ direction. The Eulerian model developed in this paper has however some special features over and above a "standard" level set technique, and these features are described below.

(a) Eulerian model derivation

The Eulerian model uses the front propagation velocity $\mathbf{U} = (u, v) = \dot{\mathbf{x}}$ such that $\mathrm{d}x/\mathrm{d}t = u$ and $\mathrm{d}y/\mathrm{d}t = v$. Here u and v are propagation velocities in x and y direction, respectively. The Eulerian model is formulated by a system of Hamilton-Jacobi equation as follows

$$\frac{\partial\phi}{\partial t} + u\frac{\partial\phi}{\partial x} + v\frac{\partial\phi}{\partial y} = 0, \tag{3.2}$$

where the front is expressed implicitly as zero level set of the solution variable $\phi = \phi(x, y, t)$, which depends on time and two spatial dimensions. It takes positive values on the right side of the front, $(\phi > 0)$, a zone which corresponds to the liquid, and it takes negative values on the left side, $(\phi < 0)$, a zone which corresponds to the foam, see Figure 2.

The time evolution of ϕ is determined in the two space dimensions by the corresponding front propagation velocity $\mathbf{U}$ with components u and v. The velocities correspond to those established in the Lagrangian model:

$$\mathbf{U} = \begin{pmatrix} u \\ v \end{pmatrix} = \frac{y}{s}\mathbf{n}. \tag{3.3}$$

For the Eulerian model the normal $\mathbf{n}$ of the propagating front is determined as [16]

$$\mathbf{n} = \frac{\nabla\phi}{|\nabla\phi|} = \frac{1}{\sqrt{\phi_x^2 + \phi_y^2}} \begin{pmatrix} \phi_x \\ \phi_y \end{pmatrix}, \tag{3.4}$$

where the notation $|\cdot|$ corresponds to the Euclidean norm. The complication in this model, compared to a conventional Hamilton-Jacobi system is that $\mathbf{U}$ depends on the path length s (viz. (2.3) & (2.4)). Hence the equation (3.2) is insufficient as it gives an evolution equation solely for ϕ; in fact, it is necessary to obtain an evolution equation for s also. The length of the trajectory s evolves similarly to ϕ as it convects the same way. It is still possible to determine Lagrangian particle paths, even given an Eulerian field, so the concept of path length retains its meaning. During the convection s increases according to the travelled path, incrementing at a rate $|\mathbf{U}| = \sqrt{u^2 + v^2} \equiv y/s$, according to equation (2.5). Therefore, the time evolution of s is described by a Hamilton-Jacobi equation with an source term as

$$\frac{\partial s}{\partial t} + u\frac{\partial s}{\partial x} + v\frac{\partial s}{\partial y} = \frac{y}{s}, \tag{3.5}$$

where the source term models the increment of the trajectory length. Although s can be computed globally, only values of s in the neighbourhood of $\phi = 0$ level set are required.

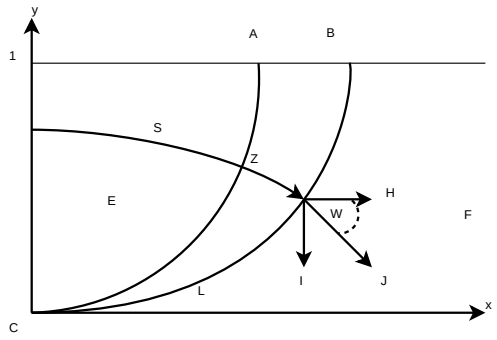

Figure 2. Dimensionless Eulerian model solution domain, with $x \in [0, \infty)$, $y \in [0, 1]$ and $t \in [0, \infty)$, showing also dependent variables ϕ and s.

With the goal of simplifying the equations, we apply the definition of the front normal as a gradient (3.4) to the definition of the velocity (3.3), which in turn is substituted into the transport equation (3.2) giving

$$\phi_t + \frac{y}{s}|\nabla\phi| = 0. \tag{3.6}$$

For the evolution of s given by the equation (3.5), we have (again substituting from (3.3))

$$s_t + \frac{y}{s}\left(\frac{\nabla\phi \cdot \nabla s}{|\nabla\phi|} - 1\right) = 0. \tag{3.7}$$

Generalizing, the system composed for equations (3.6) and (3.7), has the structure

$$\phi_t + H(y, s, \nabla\phi) = 0, \tag{3.8}$$

$$s_t + G(y, s, \nabla s, \nabla\phi) = 0, \tag{3.9}$$

where both equations, (3.8) and (3.9), have to be solved in a coupled way, with H and G as the respective Hamiltonians,

$$H = \frac{y}{s}|\nabla\phi|, \tag{3.10}$$

$$G = \frac{y}{s}\left(\frac{\nabla\phi \cdot \nabla s}{|\nabla\phi|} - 1\right). \tag{3.11}$$

The boundary conditions of the coupled system (3.8)–(3.9) are

$$\phi(t, x, y = 1) = x - \sqrt{2t}, \quad s(t, x, y = 1) = \sqrt{2t}, \tag{3.12}$$

as was established in [5] and [6], noting that the evolution of the front at the top, i.e. at $y = 1$ is described by $x = \sqrt{2t}$. On the other hand at $x = 0$, $s = 0$ and $\phi = -\sqrt{2yt}$. Since we are ultimately interested only in how the zero level set propagates, the choice of boundary conditions is non-unique, but the choices indicated here have the advantage of keeping ϕ on the boundary relatively close to being distance from the zero level set. Finally, as the model considers first order equations, we need only one boundary condition per spatial dimension (that applies to both equations (3.8) and (3.9)), whilst information propagates from the top ($y = 1$) downwards and from the left ($x = 0$) rightwards.

The initial conditions of the coupled system (3.8)–(3.9) are

$$\phi(t = \varepsilon^2/2, x, y) = x - \sqrt{y\varepsilon^2}, \quad s(t = \varepsilon^2/2, x, y) = \sqrt{y\varepsilon^2}, \tag{3.13}$$

where $\varepsilon \ll 1$. The value of ε is fixed for simulation purposes equal to just a few times the grid spacing (in section 5). A finite ε avoids the need to consider times all the way down to $t = 0$

(at which velocities are theoretically infinite). The term $\sqrt{y\varepsilon^2}$ of the initial condition (3.13) is not arbitrary, but rather arises from an early-time analytical solution, called the Velde solution, which is a good approximation for the front shape at early times ($t \ll 1$) [4,6,9]. We start with a small but non-zero ε which keeps s non-zero within the denominators of (3.6)–(3.7). This establishes that at time $t = \varepsilon^2/2$ the zero level set is situated just slightly shifted from the y axis. Intuitively results should be insensitive to ε, since equation (3.13) already incorporate an early time asymptotic behaviour of the system.

Concluding, the Eulerian model to solve consists of the equation system (3.8)–(3.9) together, with the corresponding initial and boundary conditions.

4. Numerical scheme

In this section the numerical method to solve the presented mathematical model in the form of a strongly coupled system of Hamilton-Jacobi equation is outlined. We remark that in the present work a full description is given of the methodology used to obtain some preliminary Eulerian data presented by [7]. The numerical methods were *not* themselves presented in [7].

In order to obtain a numerical solution of the mathematical model and a computational simulation of the foam-liquid displacement process, first a discrete approximation of the equations (3.8) and (3.9) is needed. A finite volume scheme is used, applying an upwind flux according to [17]. This section continues as follows: first in (a) the spatial discretization is described, in (b) the numerical flux for ϕ and s is given, in (c) the reinitialization is introduced and how it is used in the numerical simulation is described, and finally in (d) it is explained how the orientation angle α and curvature κ are measured for the propagation front.

(a) Spatial discretization

For the spatial discretization the domain in the x and y direction is divided, for simplicity, into N_x and N_y elements of equal width $\triangle x$ and $\triangle y$, respectively. Also, the domain is enlarged on all sides of the rectangle. In the x direction it is incremented by $\triangle x/2$ on each side, and in the y direction by $\triangle y/2$ on each side. This is done so that the corners of the domain are included as the centre of the corresponding volume elements generated. For illustration see Figure 3, where X denotes the maximum distance at which the position of the front is required, and the points $(0,0)$, $(0,1)$, $(X,0)$ and $(X,1)$ are centre nodes of their surrounding volume elements.

(b) Numerical flux

In order to solve the governing equations in the form of a two-dimensional system of two strongly coupled Hamilton-Jacobi equations, we use a coupled finite volume scheme, with an upwind flux, the flux being the numerical approximation of equations (3.10) and (3.11) [17].

According to the scheme, in time step t^n, the variable is reconstructed by a piecewise polynomial and evolved to time step t^{n+1}. For the stepwise numerical solution one assumes that the discrete approximation in the nodes (j,k) at time $t = t^n$ is given by $\phi^n_{j,k} \approx \phi(x_j, y_k, t^n)$. To evolve the solution at these points to time $t = t^{n+1}$ one utilizes a fully upwind version of the numerical flux of [17], which establishes that ϕ and s evolve at a rate

$$\frac{\mathrm{d}}{\mathrm{d}t}\,\phi_{j,k}(t) = H(y, s, \phi_x^-, \phi_y^+), \qquad \frac{\mathrm{d}}{\mathrm{d}t}\,s_{j,k}(t) = G(y, s, \phi_x^-, \phi_y^+, s_x^-, s_y^+), \tag{4.1}$$

respectively, where ϕ_x^-, ϕ_y^+, s_x^- and s_y^+ are the derivatives x and y in a given direction relative to the referred volume. We only need ϕ_x^-, ϕ_y^+, s_x^- and s_y^+ since for the specific curve shape as indicated in Figure 2 we expect $\phi_x > 0$ and $\phi_y < 0$, which implies that $\partial H/\partial\phi_x \geq 0$ and $\partial H/\partial\phi_y \leq 0$, and analogously for s, $\partial G/\partial s_x \geq 0$ and $\partial G/\partial s_y \leq 0$. This indicates that the numerical flux is entirely upwind. Even though the upwind flux holds for the specific front shapes

to be considered in the present work, a general numerical flux (see Appendix C) is needed in order to deal adequately with model extensions including heterogeneities and anisotropies [17].

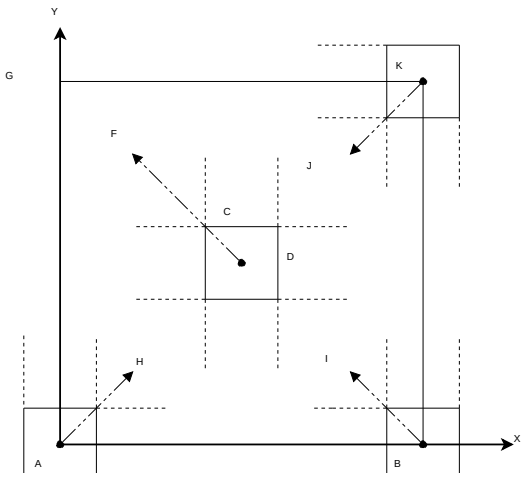

Figure 3. Spatial discretization over the domain $y \in [0, 1]$ and $x \in [0, X]$, where X is the maximum distance at which the position of the front is required. N_x and N_y are the number of partitions in x and y direction respectively: partitioned into equal sized areas ($\Delta x = \Delta y$). Here $j \in \{1, ..., N_x\}$ and $k \in \{1, ..., N_y\}$ are the coordinates of the node, associated with a value of $\phi^n_{j,k}$ at the time t^n.

In each time step, both equations for ϕ and s are evolved simultaneously. Which equation (ϕ or s) is treated first is irrelevant, because in order to obtain $\phi^{n+1}_{j,k}$ and $s^{n+1}_{j,k}$, in each case, the data for $\phi^n_{j,k}$ and $s^n_{j,k}$ are only used once.

To calculate ϕ^-_x, ϕ^+_y, s^-_x and s^+_y we suppose that we have approximated ϕ at time $t = t^n$ for all nodes. Then, we carry out a piecewise quadratic interpolation in both spatial dimensions, from which subsequently we obtain the expressions for the derivatives (see Appendix C).

For the temporal discretization of ϕ and s we use the Euler method,

$$\frac{\mathrm{d}}{\mathrm{d}t}\phi_{j,k}(t) \approx \frac{\phi^{n+1}_{j,k} - \phi^n_{j,k}}{\triangle t}, \qquad \frac{\mathrm{d}}{\mathrm{d}t}s_{j,k}(t) \approx \frac{s^{n+1}_{j,k} - s^n_{j,k}}{\triangle t}. \tag{4.2}$$

To ensure numerical stability in the evolution of the equations according to [18] one sets

$$\triangle t < \frac{\min(\triangle x, \triangle y)}{\max\{|a^-_{j,k}|, |b^+_{j,k}|\}}, \tag{4.3}$$

where $a^-_{j,k}$ and $b^+_{j,k}$ are the local propagation velocities in the x and y direction respectively (see Appendix C). The time step size is adapted according to the evolution speeds of s and ϕ by setting the Courant-Friedrichs-Levy (CFL) number to 0.475, following [17].

(c) Reinitialization

In the calculations of the Level Set Method, usually the discrete representation of the level set function develops non-smoothness during its evolution, since numerical errors increase. This impacts the structure of the solution and finally destroys the stability of the scheme [15].

To correct this, a numerical strategy is introduced, which is known as reinitialization. It restores the regularity of ϕ and stabilizes its time evolution. The reinitialization is done after each time step. Then the degraded solution ϕ is converted into a distance function, see [12]. This distance function measures the distance to the zero level set such that its absolute value

corresponds to this distance, and its sign is retained. One method to realize the reinitialization is to solve the evolution equation obtained in [15], namely

$$\frac{\partial \phi}{\partial t'} = \text{sign}(\phi)(1 - |\nabla \phi|), \tag{4.4}$$

where t' is the "artificial" time, sign(ϕ) is a sign function which takes the value 1 in the region where $\phi > 0$, -1 where $\phi < 0$, and 0 on the interface $\phi = 0$ level set. Smooth behaviour of ϕ is not guaranteed, since the interface itself is computed numerically [15]. In this work, the method suggested in [19] is used, where equation (4.4) is solved, but the numerically smoothed version of the sign function

$$\text{sign}(\phi) = \phi(\phi^2 + |\nabla \phi|^2 (\triangle x)^2)^{-1/2}, \tag{4.5}$$

is used. Note that the equation (4.5) works reliably for a square spatial partition, i.e. $\triangle x = \triangle y$, that corresponds (for most of the calculations to be considered here) to the case of the present solution. During the application of the reinitialization using this equation, the value of sign(ϕ) needs to be constantly updated during the evolution of ϕ, that evolves in time until a steady state is reached, typically in two artificial time steps (t') if the reinitialization is executed in each time step (t). The reinitialization helps to obtain a notably smoother shape of the front and in particular for the front curvature.

(d) Calculation of front orientation angle α and curvature κ

As was mentioned before, the Eulerian and Lagrangian model results can be compared via the orientation angle and the curvature along the front, in addition to comparing the front location. The angle α is the angle measured between the normal $\mathbf{n}$ of the front and the horizontal straight line parallel to x axis and the curvature κ is a spatial derivative of this.

To compute the orientation angle at all points of a front for a given time t, first, an explicit representation (x_i, y_i), $i \in \{1, ..., N_y\}$ of points on the front is obtained from the implicit representation by the curves of level zero by a linear interpolation of the data of ϕ.
From these points on the front the angle is approximated as

$$\alpha_i = \arctan\left(\frac{x_i - x_{i+1}}{y_i - y_{i+1}}\right), \qquad i \in \{1, ..., N_y - 1\}.$$

Once the orientation angle α for each point on the front is calculated, the curvature can be estimated as (see equation (B.9) in Appendix B)

$$\kappa_i = \frac{\alpha_{i+1} - \alpha_i}{\sqrt{(x_i - x_{i+1})^2 + (y_i - y_{i+1})^2}} \qquad i \in \{1, ..., N_y - 1\}.$$

Another way to obtain the curvature, which is used in this work following [15], is to calculate it in terms of ϕ by the function

$$\kappa = \frac{\phi_{yy}\phi_x^2 - 2\phi_x\phi_y\phi_{xy} + \phi_{xx}\phi_y^2}{(\phi_x^2 + \phi_y^2)^{(3/2)}}. \tag{4.6}$$

Both α and κ are calculated numerically for grids of various different resolutions. The results are shown in the next section.

5. Results

In this section, results of the computational simulation of the Eulerian model of the system of equations (3.8) and (3.9) are presented in comparison to the (Lagrangian) pressure-driven growth model. Specifically the front shape, the front orientation angle α and the curvature κ are shown compared with the analytical solutions of [4] and [7]. First in (a) we present the numerical results of the front shape, in (b) the front orientation angle α is shown revealing the presence of a concave corner or kink, in (c) the computation of the curvature κ is shown, and finally in

(d) the numerical representation for the movement of the kink through the front is given as a function of the time.

(a) Front shape

The front shape obtained by the computational simulation of the Eulerian model given by the system of two Hamilton-Jacobi equations (3.8) and (3.9) is shown in Figures 4 and 5. The simulations are realized with a $N_x = N_y = 200$ grid. In Figure 4(a) the values of solution ϕ at time $t = 0.5$, over the domain $(x, y) \in [0, 1]^2$ are shown, and the intersection of ϕ with the xy plane, which represents the propagating foam-liquid front, where $\phi = 0$, is highlighted. An explicit representation of the front is shown in Figure 4(b), where the values of ϕ for the zero level set and on both sides are indicated. In Figure 5 one can see that the numerical solutions of the Eulerian model are visually similar to the results of the (Lagrangian) pressure-driven growth model, independently of the time.

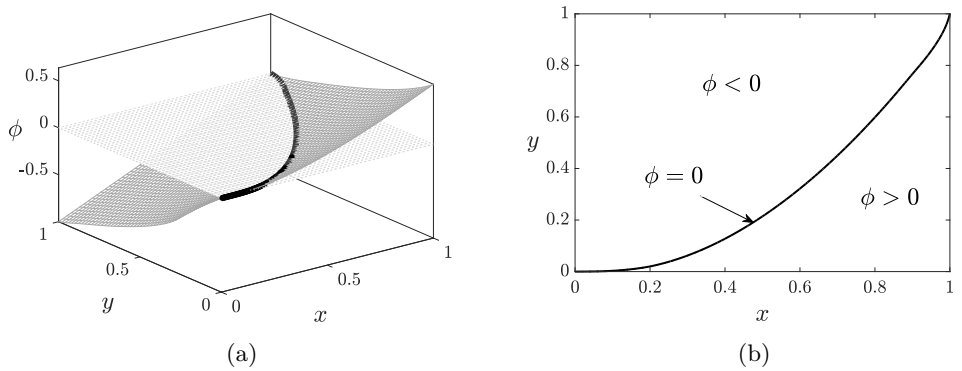

Figure 4. Foam-liquid front at evolution time $t = 0.5$ over the domain $0 \le x \le 1$, $0 \le y \le 1$. (a) Intersection of surface ϕ with plane xy. (b) Contour line of zero level set $\phi = 0$.

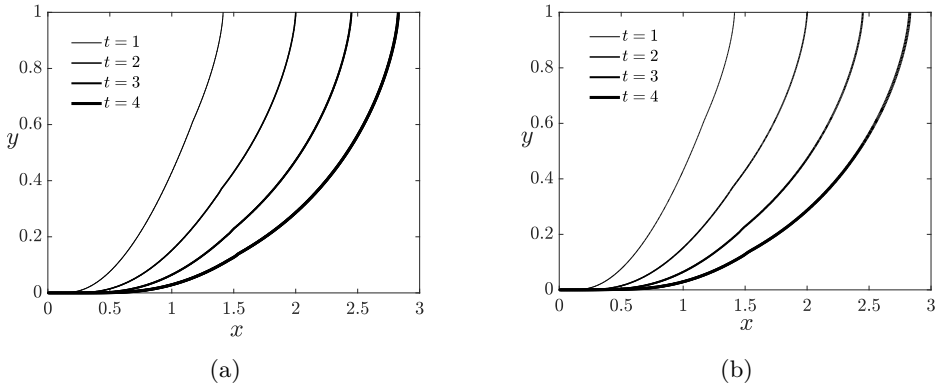

Figure 5. Front position on domain $(x, y) \in [0, 3] \times [0, 1]$. (a) Pressure-driven growth, (b) Eulerian model.

The model has been set up using an early asymptotic solution (as was established by the equation (3.13)), in such a way that ε should have hardly any bearing on the results.

In order to verify the limited effect of ε in the front shape, we have calculated the front position for $\varepsilon \in [10^{-2}, 10^{-3}, 10^{-4}]$ from time $t = \varepsilon^2/2$ to time $t = \hat{\varepsilon}^2/2$ (with $\hat{\varepsilon} = 10^{-1}$). The front displacement error (averaged over the length of the front) compared with the known asymptotic analytical solution at time $t = \hat{\varepsilon}^2/2$, for each ε studied, is equal to 7.49×10^{-4}, 8.01×10^{-4} and 8.05×10^{-4}, which, given that the top of the front has already displaced by $\hat{\varepsilon}$, implies a good agreement at early times and consequently at later time also. It was also found, measuring the absolute error, that the order of convergence (respect to spatial refinement) of the solution is approximately equal to 2, which is in concordance with the numerical method used [17].

As was mentioned before, at the top of the front ($y = 1$) the orientation angle $\alpha = 0$, however, it turns out that immediately below the top it grows like square root of distance from the top [4]. As a result, the angle can be quite significant even at relatively small distance below the top. This can be difficult to appreciate in Figure 4(b), but it becomes clear when measuring the front orientation angle α (see Figure 7).

Specifically in Figure 5 the data obtained with the (Lagrangian) algorithm and numerical parameter values in [4] are compared with those of the computational simulation using the Eulerian model for times $t \in \{1, 2, 3, 4\}$. The agreement seen between data from the original Lagrangian model (Figure 5(a)) and the Eulerian model (Figure 5(b)) suggests that the Eulerian model is being computed correctly.

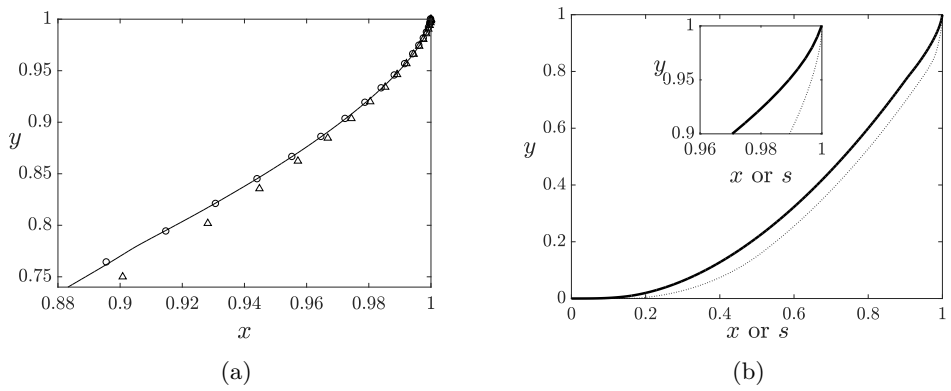

Figure 6. (a) Zoom on domain $(x, y) \in [0.88, 1] \times [0.74, 1]$ for $t = 0.5$. Solid line: Numerical results by solving Hamilton-Jacobi equation system. "△": Analytical solution from [7], taking $c = 1$ (see Appendix B). "∘": Analytical solution from [7], taking $c = 0.75$ (see Appendix B). (b) Position of foam-liquid front and trajectory length at $t = 0.5$ over domain $(x, y) \in [0, 1]^2$, calculated with a $N_x = N_y = 200$ grid. Dotted line: length of trajectory s. Solid line: Front position.

In Figure 6(a) the numerical solution for the Hamilton-Jacobi equation system is plotted for the points near to the top boundary. This is done in order to make a comparison between the Eulerian model and an approximate analytical similarity solution, developed in [7]. This similarity solution depends on a parameter c. Since s is approximately equal to x near the top, and since $2c - 1$ is defined as the ratio between $\mathrm{d}s/\mathrm{d}y$ and $\mathrm{d}x/\mathrm{d}y$, it might be thought naively that $c = 1$. However this ignores the fact that both $\mathrm{d}s/\mathrm{d}y$ and $\mathrm{d}x/\mathrm{d}y$ are equal to zero at the top. When the problem is formulated correctly, it is possible to show that $c = 0.75$ right at the top, and moreover (using an integro-differential approach presented in [7]) the value of c is very insensitive to the vertical location, moving downwards from the top. The form of those similarity expressions can be found in Appendix B and as seen in Figure 6(a), the case $c = 0.75$ gives an excellent fit. To corroborate this, in Figure 6(b) the position of points x on the front is compared to the length of trajectory s, i.e. for given value of y (and for a given value of t) the

magnitude of x and s is shown. For all material points the trajectory length s is greater than the front displacement x because points move both downwards and sideways. Even at the top $y \approx 1$, where $s \approx x$, we observe that $\mathrm{d}s/\mathrm{d}y$ is less than $\mathrm{d}x/\mathrm{d}y$, as was deduced in [7]. Since the ratio between $\mathrm{d}s/\mathrm{d}y$ and $\mathrm{d}x/\mathrm{d}y$ equals $2c-1$, it is clear that c is less than 1 near the top.

(b) Front orientation angle α

For a more stringent comparison between our Eulerian numerical data and predictions of the early-time asymptotic theories, the orientation angle and the curvature are measured. Note that the front orientation angle is zero at the top of the front ($y=1$) at all times, and approaches $\pi/2$ at the bottom of the front ($y=0$) at least in the limit of long times. Figure 7 (solid line) shows the Eulerian data of the orientation angle α at time $t=0.5$ over the domain $[0,1]\times[0,1]$ with a grid $N_x = N_y = 400$.

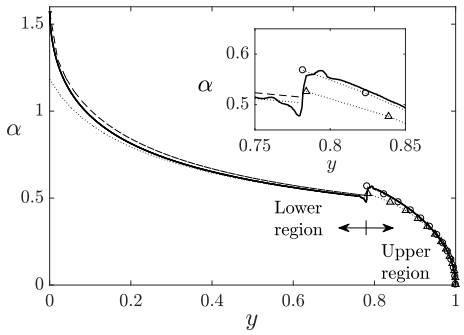

Figure 7. Front orientation angle α of the numerical Eulerian model (solid line, with $N_x = N_y = 400$ grid) vs analytical solutions for $t=0.5$ on domain $(x,y)\in[0,1]^2$. For the lower region the improved Velde solution, equation (A.3) (dotted line) and the Velde solution (dashed line) are plotted. In the upper region, two analytical expressions from [7] are plotted: ("△") $c=1$ and ("○") $c=0.75$ (see Appendix A and B).

The front shapes presented in section 5(a) are continuous and can be resolved with a few grid points ($N_x = N_y = 200$ grid in the case of section 5(a)), whereas for derivative quantities like the front orientation angle α and curvature κ (which exhibit discontinuities) a refined grid is necessary to resolve the location of the jump (Figure 8 shows the effect of having a low resolution in such a case). In Figure 7, a jump or discontinuity in the front orientation angle α around location $y \approx 0.78$ can be seen at this time ($t=0.5$). This situation has already been discussed in [7]. It corresponds to the foam front reorienting itself on a small distance comparable with the thickness of the finely-textured foam front (rather than comparable with the much longer length scale over which the front has propagated). The jump or discontinuity in α arises due to an incompatibility between material points which have continuously been on the foam front since time zero (which are unaware of the top boundary condition) and material points which have been newly injected from the top boundary since time zero (and which are influenced by the top boundary condition). This corresponds to a concave corner in the x versus y representation of the front albeit one that is not easy to recognize in Figure 6.

We refer to the points above the concave corner as the "upper" region and points below it as the "lower" region. Approximate analytical formulae (see Appendix A and B) are available to describe each region. Figure 9 shows good agreement between numerical and analytical results in each case.

Even though the angle α is sufficient to show how similar the new Eulerian solution is to the Lagrangian representation of the front considered by [7] and also sufficient to show the appearance of a jump in the angle (strong evidence of a concave corner as per [7]), in order to obtain an even more stringent test of the Eulerian formulation the curvature is measured in the next subsection.

(c) Front curvature κ

Owing to the jump in the angle, we expect the curvature to be large and negative at the jump point (specifically to scale inversely with the grid spacing in our numerical scheme). There may also be some numerical diffusivity [20], causing points near the jump to be affected as well. In Figure 8 the numerical values of the curvature obtained by the Eulerian numerical simulation of the front propagation is shown for $t = 0.5$ with grid partitions $N_x = N_y = 100$ (Figure 8(a)) and $N_x = N_y = 800$ (Figure 8(b)) over the domain $(x, y) \in [0, 1]^2$. Unsurprisingly the curvature computed at the jump itself becomes more significant if the grid is refined. Moreover, oscillations in the values of curvature κ appear close by the jump, but these appear to be numerical artifacts. What is of more interest here however is how the curvature computed via equation (4.6) changes away from and on the approach to the jump.

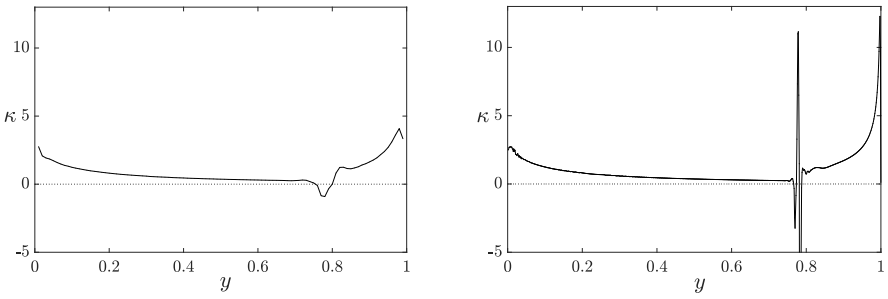

Figure 8. Curvature κ for two different grid refinement levels at the time $t = 0.5$. (a) $N_x = N_y = 100$ and (b) $N_x = N_y = 800$.

As can be seen in Figures 8 and 9 the curvature is largest near the top and bottom of the domain, but decreases on the approach to the jump. Because of its location (in an otherwise comparatively low curvature region), the behaviour at the jump could be misinterpreted, for the Lagrangian method, as a consequence of possible misplacement of material points. Under such circumstances, a convex front shape can be switched to a concave one merely by very small point misplacements. The Eulerian model (which does not require that the material points be tracked) does not suffer from this disadvantage, and moreover in Figure 9 is seen to agree with approximate analytic curvature predictions (see Appendix A and B).

(d) Jump position as function of time

In Figures 7, 8 and 9, it was possible to examine the location of the jump or discontinuity (identified as the steepest part locally on the α versus y curve) with different grid points over the same domain at the same time, and this situation was also compared with some analytical expressions for the front itself, in both the lower region and the upper region. The interesting aspect here is to analyse how the location of the jump evolves with time. This fact was already mentioned in [7], where it was established that the location of the jump would be at

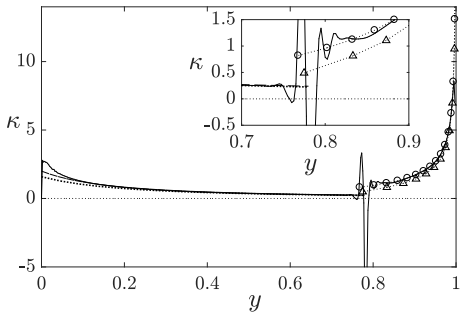

Figure 9. Front curvature κ of the numerical Eulerian model (solid line, with $N_x = N_y = 400$ grid points) vs analytical solutions for $t = 0.5$ on domain $(x, y) \in [0, 1]^2$. For the lower region, equation (A.4) (dotted line) and the Velde solution (dashed line) are plotted. In the upper region, two analytical expressions deduced from [7] are plotted: ("△") $c = 1$ and ("∘") $c = 0.75$ (see equation (B.10) in Appendix B).

$y = 1 - 0.954t/2 + O(t^2)$. This was predicted via a similarity solution, but not validated against numerical data.

Numerical data are presented here in Figure 10. Specifically 10(a) examines how the front orientation angle α as a function of height y evolves over time. In Figure 10(b) it is shown how the jump moves in the y direction (solid line) as a function of time, the jump position heuristically being detected as the position of the steepest positive derivative of the angle.

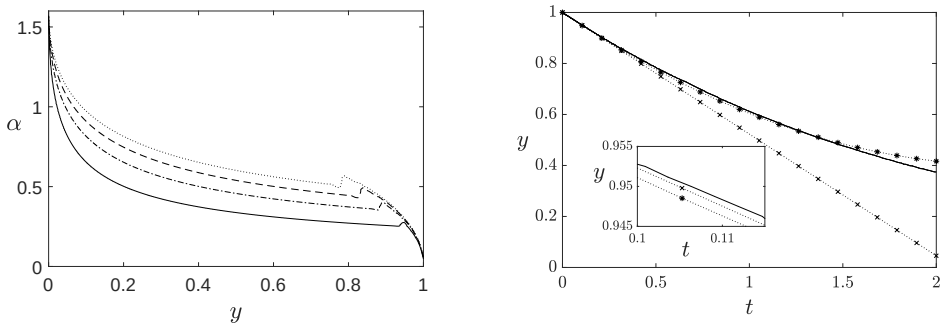

Figure 10. (a) Orientation angle α for different times, over the domain $(x, y) \in [0, 1] \times [0, 1]$ with $N_x = N_y = 400$. Dotted line: $t = 0.5$, dashed line: $t = 0.375$, dot-dashed line:$t = 0.25$, solid line: $t = 0.125$. (b) Jump position y as a function of the time t (over the domain $(x, y) \in [0, 2] \times [0, 1]$) for the Eulerian data (solid line, grid of $N_x = 800$ and $N_y = 400$) and the position y of material points initially just beneath the top determined by the equation (A.2), with initial vertical location $y_0 \to 1$ ("$*$"), and equation $y = 1 - 0.954t/2$ ("$\times$") discussed in [7].

In the Lagrangian picture, as points are injected from the top, it is thought that the concavity is a result of the collision of those injected points with those originally along the y-axis (see Figure 11). The movement of the jump through y over the time can be fit via a parabola with the form of

$y = 1 + a_1 t + a_2 t^2$, where the parameters a_1 and a_2 were found through interpolation. The fitted parameters after interpolation within the interval $t \in [0, 2]$ over the domain $(x, y) \in [0, 2] \times [0, 1]$ are $a_1 = -0.4635$ and $a_2 = 0.0784$, which vary only very slightly from equation (A.2). The fact that, for much of the evolution, the predicted location of the jump according to the curve fit is very slightly below what is predicted by equation (A.2) which gives the location of the material point initially at the top of the front. This is the opposite of what was found in [7] via a first order theory out to order t. Equation (A.2) is however itself just an asymptotic expansion (albeit now to second order not first order). The zoomed inset in Figure 10(b), at early time $t \approx 0.1$, shows the prediction of (A.2) being below the first order prediction for the jump location, but the numerical jump location is above either of them. Whether the location of the jump is above or below the location of the uppermost material point initially on the front is inconclusive, but what is clear is that these two locations are close to one another and they can only be distinguished numerically using a high resolution grid.

6. Conclusions

We have simulated the shape of a foam-liquid front evolving via pressure-driven growth but using an Eulerian model. The simulation results of the Eulerian model are largely similar to the Lagrangian results of [4]. Good agreement, not only between Eulerian and Lagrangian models, but also between Eulerian results and an asymptotic analytical solution from [7] were found. These results mutually validate all these various methods, in particular those with respect to front orientation angle and front curvature, see Figures 5, 7 and 9.

With the developed computational code, systems of Hamilton-Jacobi equations are solved. As a guideline for spatial discretization and explicit time discretization by the Eulerian method as a reference the work of [17] was taken. In the Eulerian model the front representation is determined implicitly as a zero level set. This implicit representation liberates us from the necessity to inject material points explicitly onto the front from the top, as would be required by the simulation of the Lagrangian model, making the Lagrangian model susceptible to errors in the event that those newly injected points are wrongly placed.

Though the Eulerian solution is implicit, expressing the front position as the zero level set of the solution variable ϕ, one can obtain an explicit representation of the location of the front for each time instant. From the data obtained by the numerical solution of the Eulerian model, one can detect a jump or kink in the front orientation angle. This gives evidence of the existence of a sharp concavity in the front. This is also evident by the curvature becoming large and negative at the jump. This concavity can be interpreted as a consequence of the information from the top boundary condition ($\phi(x, y = 1, t) = x - \sqrt{2t}$) propagating into the solution domain and being distinct from that associated with points originally on the front.

From the analytical calculations, it can be confirmed that the concavity is close to height $y \approx 1 - 0.4635t + 0.0784t^2$, for $t \leq 2$. This equation predicts a location that is very close to the vertical position of a material point originating on the y-axis immediately below the top boundary. As alluded to above, the concavity actually occurs at the point at which material points coming from the top boundary manage to arrive, assuming they are injected early on in the evolution. Since we have analytical approximations to the both zones of the front (points originally on the front and newly injected ones) it is possible to estimate where they join [7].

Appendix A. Asymptotic analytic solution of Lagrangian model

In what follows the early-time analytic solution of the Lagrangian model presented in [6] is recalled. This solution reflects the fact that at the top, for any time ($t > 0$), $\alpha = 0$ and $s = x$, and for any point on the front, for small times ($t \ll 1$), that $s \approx x$ and $\alpha \approx 0$. On the top, for $t > 0$, the model (2.3) reduces, after integration, to $x = \sqrt{2t}$, and for any point on the front, for $t \ll 1$ to $x \approx \sqrt{2yt}$, termed the Velde solution by [7]. Using the property that $\sin(\alpha) \approx \mathrm{d}x/\mathrm{d}y$ (for

$\mathrm{d}x/\mathrm{d}y \ll 1$) and differentiating $x \approx \sqrt{2yt}$ with respect to y gives $\sin(\alpha) \approx \sqrt{t/2y}$. Putting this in the equation (2.4) gives, after integration,

$$y \approx y_0 - t/2, \tag{A.1}$$

where y_0 is the initial position of a given material point. Equation (A.1) describes material points which originate anywhere below the top $y_0 \leq 1$ and move with a vertical velocity $-1/2$. A higher order correction was also obtained by [7] still assuming $t \ll 1$

$$y \approx y_0 - \frac{t}{2} + \frac{5t^2}{48y_0}. \tag{A.2}$$

Equation (A.1)−(A.2) have implications for schemes for solving the Lagrangian model numerically (details of such schemes can be found in literature [4]). Owing to (A.1) and (A.2), a gap opens up between the point at the top of the front (which remains on the top boundary for all time) and material points slightly underneath it (those with $y_0 \to 1$) which necessarily drift downwards: in the Lagrangian model, new material points (hereafter called "newly injected points") must continually be injected from the top boundary to fill this gap. Upon leaving the top boundary their downwards velocity component starts off small, but grows over time to ensure that the gap is filled [7]. The gap between the top of the front and the material points that started off immediately below it meanwhile becomes wider and wider over time, such that over time, more and more of the front is comprised of newly injected points (see Figure 11).

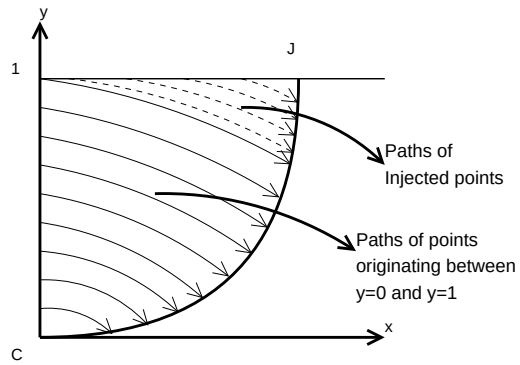

Figure 11. Distinction between trajectories of points originally at $x = 0$ in $0 \leq y \leq 1$, and points injected at the top $y = 1$ for $x > 0$. In the Lagrangian formulation, to resolve the front shape near the top we need to add new material points to replace those originally on the front that have drifted downwards. However we do not know where exactly to add them unless we already know the shape of the front.

Using equation (A.1) it is possible to improve upon the estimate that $x \approx \sqrt{2yt}$, specifically by obtaining the "improved Velde" solution discussed in [7] which established that $x \approx \sqrt{2yt + t^2/6}$. This equation will be used in section 6 to compare the orientation angle and the curvature of the front in the, so-called, "lower region" of the front [7]. The lower region extends downwards from the position where the original front points and the injected front points meet, whereas the "upper region" extends from this point upwards. Since, using (2.2), $\alpha = \arctan(\mathrm{d}x/\mathrm{d}y)$, it is possible to derive a formula for the curvature in the lower region, the curvature being given by $\kappa = -(\mathrm{d}\alpha/\mathrm{d}y)\cos(\alpha)$ (see equation (B.9) in Appendix B), so that

$$\alpha \approx \arctan\left(t(2yt + t^2/6)^{-1/2}\right), \tag{A.3}$$

$$\kappa \approx 6^{3/2}\sqrt{t}(12y+7t)^{-3/2}. \tag{A.4}$$

For the upper region it is possible to obtain, using the similarity equation developed in [7], an analytical approximation of the front position (see Appendix B). However the resulting formulae for front orientation angle and curvature are less simple than in (A.3) and (A.4). Nonetheless, the angle and the curvature can be estimated for both, the "lower" and "upper" region.

Appendix B. Front shape in the upper region

Using the similarity equations developed in [7] it is possible to obtain a parametric analytical expression for the upper region of the front in terms of $x = x(t, \Xi)$ and $y = y(t, \zeta)$, where Ξ and ζ are the rescaled form of x and y, respectively. Here we recall and extend the results of [7]. If we assume from [7] that

$$\Xi = (\sqrt{2t} - x)t^{-3/2} \equiv \xi t^{-3/2}, \tag{B.1}$$

$$\zeta = 2(1-y)/t, \tag{B.2}$$

where $t \ll 1$, and also that the orientation angle can be expressed as $\alpha = \sqrt{t/2}\,A(\zeta)$, then [7] demonstrates

$$\zeta \approx \frac{(1-cA)^{1/c}}{(1-c)} - \frac{(1-cA)}{c(1-c)} + \frac{1}{c}, \tag{B.3}$$

where $2c-1$ is the assumed constant ratio between $\mathrm{d}s/\mathrm{d}y$ and $\mathrm{d}x/\mathrm{d}y$ in the upper region [7]. For small times ($t \ll 1$) it is possible to obtain from [7] that

$$\xi \approx -\int_y^1 \left(\alpha + \frac{\alpha^3}{3}\right) \mathrm{d}y. \tag{B.4}$$

If we combine (B.1) and (B.4), using the derivative of (B.2) respect to y ($\mathrm{d}y/\mathrm{d}\zeta = -t/2$), and also with $\alpha = \sqrt{t/2}\,A$ we obtain

$$\Xi = \frac{\xi}{t^{3/2}} \approx -\frac{1}{t^{3/2}}\int_y^1 \left(\alpha + \frac{\alpha^3}{3}\right) \mathrm{d}y = \frac{1}{2\sqrt{2}}\int_0^A \left(A + \frac{t}{6}A^3\right)\frac{\mathrm{d}\zeta}{\mathrm{d}A}\,\mathrm{d}A, \tag{B.5}$$

where $\mathrm{d}\zeta/\mathrm{d}A$ can be obtained from (B.3). In order to compare the results obtained in [7] with the Eulerian data obtained here we need to use the same values of c as used in [7], i.e. $c = 1$ and $c = 0.75$. Equation (B.3) is plotted in Figure 7, and (B.3) and (B.5) taken together are plotted in Figure 6. For $c = 1$ we have via equation (B.3) that (taking the limit when $c \to 1$ of ζ)

$$\zeta = (1-A)\log(1-A) + A, \tag{B.6}$$

then differentiating (B.6) respect to A we can compute, using equation (B.5), that

$$\Xi \approx -\frac{1}{2\sqrt{2}}\int_0^A \log(1-A)\left(A + \frac{t}{6}A^3\right)\mathrm{d}A. \tag{B.7}$$

Now, combining equations (B.1) with (B.6) and (B.2) with (B.7), for each value of A we can obtain Ξ and ζ, and thus, x and y. The range of A values is easy to obtain owing to the fact that ζ is the rescaled version of y, i.e. when $\zeta = 1$, $y = 1 - t/2$ (cf. early-time solution (A.1)) and when $\zeta = 0$, $y = 1$. Thus α varies from 0 to $\sqrt{t/2}$ and A varies from $A = 0$ ($\zeta = 0$) to $A = 1$ ($\zeta = 1$) at least in this case $c = 1$ (one of the cases of interest in Figure 6).

The same procedure as used to obtain equation (B.7) can to be used in order to obtain the analytical expression for Ξ for values of $c < 1$. As a result we obtain

$$\Xi \approx -\frac{1}{2\sqrt{2}}\int_0^A \left(\frac{(1-cA)^{1/c}+cA-1}{(c-1)(cA-1)}\right)\left(A+\frac{t}{6}A^3\right)\,\mathrm{d}A. \tag{B.8}$$

Then, combining equations (B.1) with (B.8) and (B.2) with (B.3), for each value of A we again obtain Ξ and ζ, and x and y. Here as explained in [7], A varies from $A=0$ to $A=1.18$.

Given an expression for α in the upper region (where recall, $\alpha=\sqrt{t/2}\,A$) it is possible to obtain an analytical formula for the front curvature using the equation (B.3), then with $\kappa=-\mathrm{d}\alpha/\mathrm{d}S$, where S is the length measured along the front, we obtain

$$\kappa=-\frac{\mathrm{d}\alpha}{\mathrm{d}y}\frac{\mathrm{d}y}{\mathrm{d}S}=-\frac{\mathrm{d}\alpha}{\mathrm{d}y}\cos(\alpha), \tag{B.9}$$

then substituting the similarity solution (B.3) into (B.9) we can deduce that

$$\kappa\approx\left(\frac{2}{t}\sqrt{\frac{t}{2}}\frac{1}{\mathrm{d}\zeta/\mathrm{d}A}\right)\cos\left(\sqrt{\frac{t}{2}}A\right)\approx-\left(\frac{\sqrt{2}(c-1)(cA-1)}{((1-cA)^{1/c}+cA-1)\sqrt{t}}\right)\left(1-\frac{tA^2}{4}\right), \tag{B.10}$$

which was plotted in Figure 9.

Appendix C. Semidiscrete central-upwind scheme

Although it turns out that the central-upwind flux is not strictly required in this work, it is presented here because this scheme is useful (and essential) in heterogeneous and/or anisotropic systems, which are of physical interest in improved oil recovery [9]. We start from [17]

$$\begin{aligned}\frac{\mathrm{d}}{\mathrm{d}t}\phi_{j,k}(t)=\;&-\frac{a^-_{j,k}b^-_{j,k}H^{++}-a^-_{j,k}b^+_{j,k}H^{+-}-a^+_{j,k}b^-_{j,k}H^{-+}+a^+_{j,k}b^+_{j,k}H^{--}}{(a^+_{j,k}-a^-_{j,k})(b^+_{j,k}-b^-_{j,k})}\\&-\frac{a^+_{j,k}a^-_{j,k}}{a^+_{j,k}-a^-_{j,k}}\left(\phi^+_x-\phi^-_x\right)-\frac{b^+_{j,k}b^-_{j,k}}{b^+_{j,k}-b^-_{j,k}}\left(\phi^+_y-\phi^-_y\right),\end{aligned} \tag{C.1}$$

and

$$\begin{aligned}\frac{\mathrm{d}}{\mathrm{d}t}s_{j,k}(t)=\;&-\frac{a^-_{j,k}b^-_{j,k}G^{++}-a^-_{j,k}b^+_{j,k}G^{+-}-a^+_{j,k}b^-_{j,k}G^{-+}+a^+_{j,k}b^+_{j,k}G^{--}}{(a^+_{j,k}-a^-_{j,k})(b^+_{j,k}-b^-_{j,k})}\\&-\frac{a^+_{j,k}a^-_{j,k}}{a^+_{j,k}-a^-_{j,k}}\left(s^+_x-s^-_x\right)-\frac{b^+_{j,k}b^-_{j,k}}{b^+_{j,k}-b^-_{j,k}}\left(s^+_y-s^-_y\right),\end{aligned} \tag{C.2}$$

where $H^{\triangle\square}:=H(y,s,\phi^{\triangle}_x,\phi^{\square}_y)$ and $G^{\triangle\square}:=G(y,s,\phi^{\triangle}_x,\phi^{\square}_y,s^{\triangle}_x,s^{\square}_y)$ for $\triangle,\square\in\{-,+\}$ (see equation (3.10) and (3.11)). The local propagation velocities $a^{\pm}_{j,k}$ and $b^{\pm}_{j,k}$ are estimated as

$$a^+_{j,k}:=\max_{\pm}(H_{\phi_x}(y,s,\phi^{\pm}_x,\phi^{\pm}_y))_+,\qquad a^-_{j,k}:=\min_{\pm}(H_{\phi_x}(y,s,\phi^{\pm}_x,\phi^{\pm}_y))_-, \tag{C.3}$$

$$b^+_{j,k}:=\max_{\pm}(H_{\phi_y}(y,s,\phi^{\pm}_x,\phi^{\pm}_y))_+,\qquad b^-_{j,k}:=\min_{\pm}(H_{\phi_y}(y,s,\phi^{\pm}_x,\phi^{\pm}_y))_-, \tag{C.4}$$

where $(\cdot)_+:=\max(\cdot,0)$ and $(\cdot)_-:=\min(\cdot,0)$. The values of $\phi^{\pm}_x$ are calculated (for any fixed y) using the following interpolating polynomial

$$\tilde{\phi}(x,t^n)=\phi^n_j+\frac{(\triangle\phi)^n_{j+\frac{1}{2}}}{\triangle x}(x-x_j)+\frac{(\triangle\phi)'_{j+\frac{1}{2}}}{2(\triangle x)^2}(x-x_j)(x-x_{j+1}),\quad x\in[x_j,x_{j+1}], \tag{C.5}$$

where $(\triangle\phi)^n_{j+\frac{1}{2}} \equiv \phi^n_j - \phi^n_{j+\frac{1}{2}}$, $\phi^n_{j+\frac{1}{2}} = (\phi^n_j + \phi^n_{j+1})/2$ and $(\triangle\phi)'_{j+\frac{1}{2}}/(\triangle x)^2$ is an approximation of the second derivative of $\phi_{xx}(x_{j+\frac{1}{2}}, t^n)$. To estimate $(\triangle\phi)'_{j+\frac{1}{2}}$ we use the minmod limiters

$$(\triangle\phi)'_{j+\frac{1}{2}} = \text{minmod}\Big(\theta\big[(\triangle\phi)^n_{j+\frac{3}{2}} - (\triangle\phi)^n_{j+\frac{1}{2}}\big], \frac{1}{2}\big[(\triangle\phi)^n_{j+\frac{3}{2}} - (\triangle\phi)^n_{j-\frac{1}{2}}\big], \theta\big[(\triangle\phi)^n_{j+\frac{1}{2}} - (\triangle\phi)^n_{j-\frac{1}{2}}\big]\Big),$$

where $\theta \in [1, 2]$ is a weighting factor, and the multivariable minmod function (for arbitrary arguments w_1, w_2,...) is defined as

$$\text{minmod}(w_1, w_2, ...) = \begin{cases} \min_j\{w_j\} & \text{if } \ w_j > 0 \ \ \forall\ j, \\ \max_j\{w_j\} & \text{if } \ w_j < 0 \ \ \forall\ j, \\ 0 & \text{otherwise.} \end{cases} \tag{C.6}$$

In this work a value of $\theta = 1.5$ is used for the minmod weighting factor [17]. Finally from (C.5) one obtains

$$\phi^-_x = \frac{(\triangle\phi)^n_{j-\frac{1}{2}}}{\triangle x} \mp \frac{(\triangle\phi)'_{j-\frac{1}{2}}}{2\triangle x}.$$

The expressions s^-_x and s^+_y are obtained in a similar way.

For the equations (C.3) and (C.4) we have from the definition of H in equation (3.10) that

$$H_{\phi_x} = \frac{y}{s}\frac{\phi_x}{|\nabla\phi|}, \qquad H_{\phi_y} = \frac{y}{s}\frac{\phi_y}{|\nabla\phi|}. \tag{C.7}$$

Moreover, it is easy to show that $(\partial/\partial\phi_x)H = (\partial/\partial s_x)G$ and $(\partial/\partial\phi_y)H = (\partial/\partial s_y)G$, i.e. $H_{\phi_x} = G_{s_x}$ and $H_{\phi_y} = G_{s_y}$, where $H_{\phi_x}, H_{\phi_y}, G_{s_x}, G_{s_y}$ denote partial derivatives (of H respectively G) with respect to ϕ_x, ϕ_y, s_x, s_y, respectively. This means that for both equations (3.8) and (3.9), the propagation velocities of the corresponding variable (ϕ and s) are the same.

For the specific curve shape as indicated in Figure 2 we expect $\phi_x > 0$ and $\phi_y < 0$, which implies that $H_{\phi_x} \geq 0$ and $H_{\phi_y} \leq 0$. This indicates that the numerical flux is entirely upwind, since the speeds $a^+_{j,k} = 0$ and $b^-_{j,k} = 0$ in (C.3) vanish. The upwind version of (C.1) and (C.2), where those terms disappear, is (see (4.1))

$$\frac{\mathrm{d}}{\mathrm{d}t}\phi_{j,k}(t) = H(y, s, \phi^-_x, \phi^+_y), \qquad \frac{\mathrm{d}}{\mathrm{d}t}s_{j,k}(t) = G(y, s, \phi^-_x, \phi^+_y, s^-_x, s^+_y). \tag{C.8}$$

Ethics. Ethics approval was not required for this research.

Data Accessibility. All results presented here are reproducible via analytical results detailed in the article and numerical algorithms (acessible via https://strathcloud.sharefile.eu/d-s0f35b6576ab48aca) and analytical methods detailed in the article and the appendices.

Authors' Contributions. C. Torres-Ulloa carried out the simulation study under S. Berres and P. Grassia's supervision. Drafting of the article was shared between CTU, SB and PG.

Competing Interests. We have no competing interests.

Funding. C. Torres-Ulloa received CONICYT Becas-Chile funding.

Acknowledgements. See funding statement above.

References

1. L. W. Lake, *Enhanced oil recovery*. Prentice Hall, Englewood Cliffs, NJ, 1989.
2. E. Tzimas, A. Georgakaki, C. G. Cortes, and S. Peteves, "Enhanced oil recovery using carbon dioxide in the European energy system," *Report EUR*, vol. 21895, no. 6, 2005.
3. J. Salager, "Recuperación mejorada del petróleo," *ULA.[S357-C]*, 2005.
4. P. Grassia, E. Mas-Hernández, N. Shokri, S. Cox, G. Mishuris, and W. Rossen, "Analysis of a model for foam improved oil recovery," *Journal of Fluid Mechanics*, vol. 751, pp. 346–405, 2014. [Online]. Available: https://doi.org/10.1017/jfm.2014.287
5. D. Shan and W. Rossen, "Optimal injection strategies for foam IOR," *SPE Journal*, vol. 9, no. 02, pp. 132–150, 2004. [Online]. Available: https://doi.org/10.2118/75180-MS
6. R. de Velde Harsenhorst, A. Dharma, A. Andrianov, and W. Rossen, "Extension of a simple model for vertical sweep in foam SAG displacements," *SPE Reservoir Evaluation & Engineering*, vol. 17, no. 03, pp. 373–383, 2014. [Online]. Available: https://doi.org/10.2118/164891-PA
7. P. Grassia, L. Lue, C. Torres-Ulloa, and S. Berres, "Foam front advance during improved oil recovery: Similarity solutions at early times near the top of the front," *Journal of Fluid Mechanics*, vol. 828, pp. 527–572, 2017. [Online]. Available: https://doi.org/10.1017/jfm.2017.541
8. E. Mas-Hernández, P. Grassia, and N. Shokri, "Foam improved oil recovery: Foam front displacement in the presence of slumping," *Colloids and Surfaces A: Physicochemical and Engineering Aspects*, vol. 473, pp. 123–132, 2015. [Online]. Available: https://doi.org/10.1016/j.colsurfa.2014.12.023
9. P. Grassia, C. Torres-Ulloa, S. Berres, E. Mas-Hernández, and N. Shokri, "Foam front propagation in anisotropic oil reservoirs," *The European Physical Journal E*, vol. 39:42, no. 4, 2016. [Online]. Available: https://doi.org/10.1140/epje/i2016-16042-5
10. P. Grassia, "Pressure-driven growth in strongly heterogeneous systems," *The European Physical Journal E*, vol. 41:10, no. 1, 2018. [Online]. Available: https://doi.org/10.1140/epje/i2018-11618-7
11. J. A. Sethian, "Fast marching methods," *SIAM review*, vol. 41, no. 2, pp. 199–235, 1999. [Online]. Available: https://doi.org/10.1137/S0036144598347059
12. C. Li, C. Xu, C. Gui, and M. D. Fox, "Distance regularized level set evolution and its application to image segmentation," *IEEE Transactions on Image Processing*, vol. 19, no. 12, pp. 3243–3254, 2010. [Online]. Available: https://doi.org/10.1109/TIP.2010.2069690
13. D. Adalsteinsson and J. A. Sethian, "A fast level set method for propagating interfaces," *Journal of Computational Physics*, vol. 118, no. 2, pp. 269–277, 1995. [Online]. Available: https://doi.org/10.1006/jcph.1995.1098
14. J. Boon, C. J. Budd, and G. Hunt, "Level set methods for the displacement of layered materials," vol. 463, no. 2082, pp. 1447–1466, 2007. [Online]. Available: https://doi.org/10.1098/rspa.2007.1827
15. S. Osher and R. Fedkiw, *Level Set Methods and Dynamic Implicit Surfaces*. Springer New York, 2006. [Online]. Available: https://doi.org/10.1007/b98879
16. S. Osher and J. A. Sethian, "Fronts propagating with curvature-dependent speed: algorithms based on Hamilton-Jacobi formulations," *Journal of Computational Physics*, vol. 79, no. 1, pp. 12–49, 1988. [Online]. Available: https://doi.org/10.1016/0021-9991(88)90002-2
17. A. Kurganov, S. Noelle, and G. Petrova, "Semidiscrete central-upwind schemes for hyperbolic conservation laws and Hamilton–Jacobi equations," *SIAM Journal on Scientific Computing*, vol. 23, no. 3, pp. 707–740, 2001. [Online]. Available: https://doi.org/10.1137/S1064827500373413
18. A. Coronel, P. Cumsille, and R. Quezada, "Un método numérico híbrido para capturar los choques en leyes de conservación escalares," *Revista Integración*, vol. 28, no. 2, pp. 111–132, 2010.
19. D. Peng, B. Merriman, S. Osher, H. Zhao, and M. Kang, "A PDE-based fast local level set method," *Journal of Computational Physics*, vol. 155, no. 2, pp. 410–438, 1999. [Online]. Available: https://doi.org/10.1006/jcph.1999.6345
20. S. Bidadi and S. L. Rani, "Quantification of numerical diffusivity due to TVD schemes in the advection equation," *Journal of Computational Physics*, vol. 261, pp. 65–82, 2014. [Online]. Available: https://doi.org/10.1016/j.jcp.2013.12.011